A&A 382, 537–553 (2002)
DOI: 10.1051/0004-6361:20011600

Astronomy & Astrophysics

Infrared observations of NGC 3603

I. New constraints on cluster radius and K_s-band luminosity function⋆

D. E. A. Nürnberger[1,2] and M. G. Petr-Gotzens[3]

[1] Institut für Theoretische Physik und Astrophysik, Univ. Würzburg, Am Hubland, 97074 Würzburg, Germany
[2] Institut de Radio-Astronomie Millimétrique, 300 rue de la Piscine DU, 38406 St. Martin-d'Hères, France
[3] Max-Planck-Institut für Radioastronomie, Auf dem Hügel 69, 53121 Bonn, Germany

Received 25 September 2001 / Accepted 8 November 2001

Abstract. We have performed deep K_s-band observations of the starburst region NGC 3603 with the infrared camera ISAAC mounted on the VLT Antu. The total area covered by our data stretches from the NGC 3603 starburst cluster towards the south up to a maximal distance of about 370″ (∼12 pc). This enables us to reconsider and redetermine the radial extent of the cluster which is found to be about 150″ ± 15″ (∼5 pc), exceeding previous estimates by a factor of 2.5. King model fits are used to disentangle the count statistics of cluster stars from those of field stars. With knowledge of the cluster radius we then construct and analyze the K_s-band luminosity function (KLF) of the NGC 3603 starburst cluster. The KLF for cluster radii >30″ is rising down to the completeness limit of our study at $K_s \sim 17^m$–$17\overset{m}{.}5$, corresponding to 1 Myr old cluster members of $\mathcal{M} \sim 0.5\,\mathcal{M}_\odot$. For the range of intermediate luminosity stars we obtain a KLF slope of $\alpha = 0.35 \pm 0.02$ which is consistent with a Miller-Scalo type initial mass function (IMF) of a ∼1 Myr old stellar cluster if one assumes a power-law index of $\beta \sim 2$ for the mass-luminosity relation of both intermediate mass main sequence stars and low mass pre-main sequence stars. At the high luminosity end the observed KLF likely flattens ($\alpha \sim 0.2$), being consistent with a Salpeter type IMF for NGC 3603's massive main sequence stars.

Key words. stars: formation – stars: pre-main sequence – stars: luminosity function, mass function – H II regions – ISM: individual objects: NGC 3603 – galaxies: starbursts

1. Introduction

Located at a distance of about 7 ± 1 kpc (Goss et al. 1972; Moffat 1974, 1983; Van den Bergh 1978; Clayton 1986; Melnick et al. 1989; Crowther & Dessart 1998; De Pree et al. 1999; Pandey et al. 2000) towards the tangential point of the Carina arm ($l \sim 291\overset{\circ}{.}6$, $b \sim -0\overset{\circ}{.}5$) NGC 3603 is one of the most luminous, optically visible H II regions in our Galaxy, with a total bolometric luminosity of $\sim 10^7\,L_\odot$ (Kennicutt 1984). Hence, it is frequently compared to the 30 Dor giant H II region in the Large Magellanic Cloud, although 30 Dor has about 7 times the total ionization flux, is about 10 times larger in diameter and about 40 times more massive (Balick et al. 1980; Kennicutt 1984; Moffat et al. 1994). Given their representative properties as well as the relatively moderate distances, both NGC 3603 and 30 Dor are considered as local templates of starburst regions in distant galaxies.

The main source of ionization in NGC 3603 is a massive cluster of OB and Wolf-Rayet stars (Goss & Radhakrishnan 1969), which shows – apart from the Galactic center region – the highest density of high mass stars known in the Galaxy (Melnick et al. 1989; Moffat et al. 1994; Drissen et al. 1995; Hofmann et al. 1995). Due to the relatively low foreground extinction of $A_V \sim 4 \ldots 5^m$ (Moffat 1983; Melnick et al. 1989) the NGC 3603 OB cluster offers the unique opportunity to study its stellar content in great detail by optical photometry and spectroscopy. Thus it is well known that the Trapezium-like system HD 97950 in the core of the cluster contains 3 luminous hydrogen-rich WNL stars, 6 O3 stars and many other late O type stars at an age of 2 . . . 3 Myr (Moffat 1983; Clayton 1986; Melnick et al. 1989; Hofmann et al. 1995).

Recent studies of NGC 3603 address several fundamental questions related to the violent environments of starburst regions: Do low mass stars form in such

Send offprint requests to: D. Nürnberger,
e-mail: nurnberg@astro.uni-wuerzburg.de

⋆ Based on observations obtained at the European Southern Observatory, Paranal, Chile under proposal number 63.I-0608A.

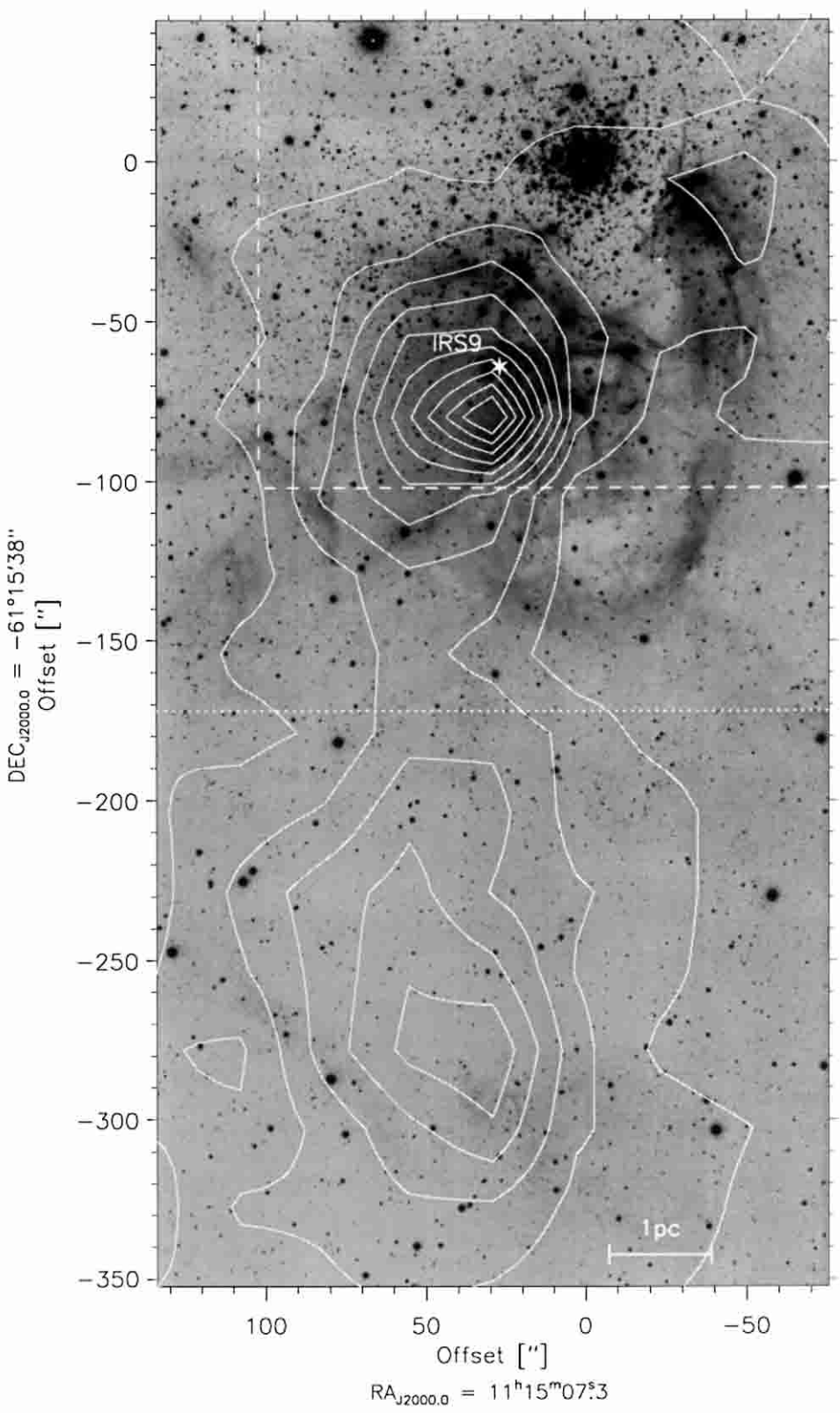

Fig. 1. Deep K_s-band image of NGC 3603 obtained with ISAAC mounted on the VLT Antu. The position of our primary target source IRS 9 is marked by an asterisk. Overlayed contour lines indicate the spatial distribution of CS (2–1) emission measured with the SEST (beam size $\sim 50''$; Nürnberger 2002b; Nürnberger et al. 2002b). The dashed line outlines the region which is overlapping with the data set of Brandl et al. (1999). The dotted horizontal line separates the northern part ($t_{\rm int}$ up to 60 min) and the southern part ($t_{\rm int}$ up to 15 min). Note that offsets are given in the cartesian coordinate system, i.e. offsets in right ascension represent $\Delta\alpha \cdot \cos(\delta)$.

environments and do they form simultaneously to the high mass stars? Does the IMF show a turnover or cut-off at low stellar masses and does its slope vary on small spatial scales? By near-infrared adaptive optics imaging of the central $13'' \times 13''$, Eisenhauer et al. (1998; hereafter E+98) studied the cluster population of intermediate and low mass stars. According to their results, there is no turnover in the initial mass function (IMF) down to $1\,\mathcal{M}_\odot$ stars but stars with less than $4\,\mathcal{M}_\odot$ appear to be younger ($\lesssim 1$ Myr) than the more massive ones. Recently, by using the *Infrared Spectrometer and Array Camera* (ISAAC) of the *Very Large Telescope* (VLT) Brandl et al. (1999; hereafter B+99) aimed to push the observational limit to subsolar masses. From their analysis of the colour-magnitude diagram and luminosity functions, they conclude that the cluster hosts a significant number of low mass stars down to $0.1\,\mathcal{M}_\odot$, assuming an age of $\sim$0.7 Myr. Due to the lack of field star reference images in both studies, these authors corrected their observed star number counts for contamination from the general Galactic field either by transfering star counts from the optical to the near-infrared (E+98), or by assuming stars located at radii $>75''$ from the cluster center as field star representatives (B+99). The latter attempt is likely based on results of Melnick et al. (1989), who determined the radius of the NGC 3603 OB cluster via *UBV* photometry of 195 luminous stars which are spread over a field-of-view of $5'.0 \times 4'.5$. They find a radius of $<$2.1 pc, corresponding to $<62''$ at the distance of 7 kpc. The populous cluster, however, may extend to radii much larger than $100''$ when less luminous stars are taken into account. Ideally, reference fields should be taken well beyond the extent of the cluster.

The VLT + ISAAC K_s-band observations presented here cover a large region ($\sim 3'.5 \times 6'.6$) of NGC 3603 with high sensitivity and sub-arcsecond spatial resolution. These data were originally obtained to search for sources which are deeply embedded in the adjacent molecular clumps. Hence the field-of-view traces the molecular line emission associated with the OB cluster. Also allowing a direct measurement of the nearby Galactic field star population, the data bear a very good potential for a new determination of both radius and luminosity function of the OB cluster. In this paper we study the radial stellar density profile of the cluster and show that it extends at least up to $\sim 150''$. Having established the cluster radius, we disentangle the count statistics of cluster stars from those of field stars and finally analyze the K_s-band luminosity function of the NGC 3603 starburst cluster. Comparison to the results of B+99 is made and implications on the IMF of the cluster are briefly discussed.

2. Observations and data reduction

During the nights 28/29 and 29/30 May 1999 NGC 3603 was observed with the infrared camera ISAAC mounted on ESO's VLT Antu and equipped with a Hawaii Rockwell 1024×1024 pixel array at a scale of $0''.147$ per pixel. The observations were performed in the broadband K_s filter ($\lambda_c = 2.16\,\mu$m, $\Delta\lambda = 0.27\,\mu$m). The target position was given by the infrared source IRS 9 (following the nomenclature of Frogel et al. 1977; $\mathrm{RA_{J2000}} = 11^h15^m11^s.34$, $\mathrm{DEC_{J2000}} = -61°16'45''.2$) which is located about $1'.2$ south of the center of the OB cluster (as defined by the mass center of the Trapezium-like system HD 97950: $\mathrm{RA_{J2000}} = 11^h15^m07^s.3$, $\mathrm{DEC_{J2000}} = -61°15'38''$; Tapia et al. 2001).

Images were acquired in a jitter pattern of 3×3 positions with typical offsets of the order $30''$. Each jitter cycle contained 10 single images, the first and the last one centered on IRS 9. The integration time per image was 1 min, consisting of 20 co-averaged frames with 3 s individual exposure time. In total, 60 images (i.e. 6 jitter cycles) were taken, resulting in an effective exposure time of 1 hour for the central $80'' \times 80''$ wide area (see the illustration in Fig. 4). Based on this very deep imaging, a detailed discussion of the stellar content around IRS 9 will be presented in a subsequent paper.

Due to the vicinity of the OB cluster all target frames show severe crowding of stars as well as large amounts of bright diffuse emission. Therefore, they could not be used to construct good sky frames. Instead, separate frames (15 images), were taken in a region located about $4'$ to the south of the OB cluster, and relatively void of stars and diffuse emission. Again a jitter scheme was applied, with each cycle containing 5 images (integration time 1 min each) offset by $\sim 60''$. These images served two purposes: they were used to construct a representative measure of the emission from the sky, and due to a small overlap with the target frames around IRS 9, also allowed the later combination of all images to a final big mosaic. The entire data set was obtained under photometric conditions and very good seeing, leading to a typical image quality of $\sim 0''.45$ FWHM measured on point-sources.

Furthermore, twilight flats as well as dark frames were taken through the usual ISAAC calibration plan. For the purpose of photometric calibration a set of faint near-infrared standard stars was observed, namely FS 19 ($K = 13.796$; Casali & Hawarden 1992), S279-F ($K = 12.026 \pm 0.006$, $K_s = 12.031 \pm 0.006$), S064-F ($K = 11.722 \pm 0.013$, $K_s = 11.724 \pm 0.007$) and S791-C ($K = 11.250 \pm 0.014$, $K_s = 11.267 \pm 0.008$; for the latter three see Persson et al. 1998).

All basic steps of data reduction were performed using routines within the IRAF and IDL software packages. First, a median sky image was created for every set of 20 target images, and carefully checked if all stars had been removed. Then the target images – including those images that were used to create the sky frames – were processed by subtracting the appropriate sky frame and dividing by a dark-subtracted median flatfield taken on the twilight sky. Finally, all images were corrected for bad pixels and registered in order to produce the final mosaic.

When inspecting this mosaic we noticed a large number of fake binary and multiple stars towards the edges and corners of the central frames as well as more or less elongated stellar intensity profiles (result of the superposition

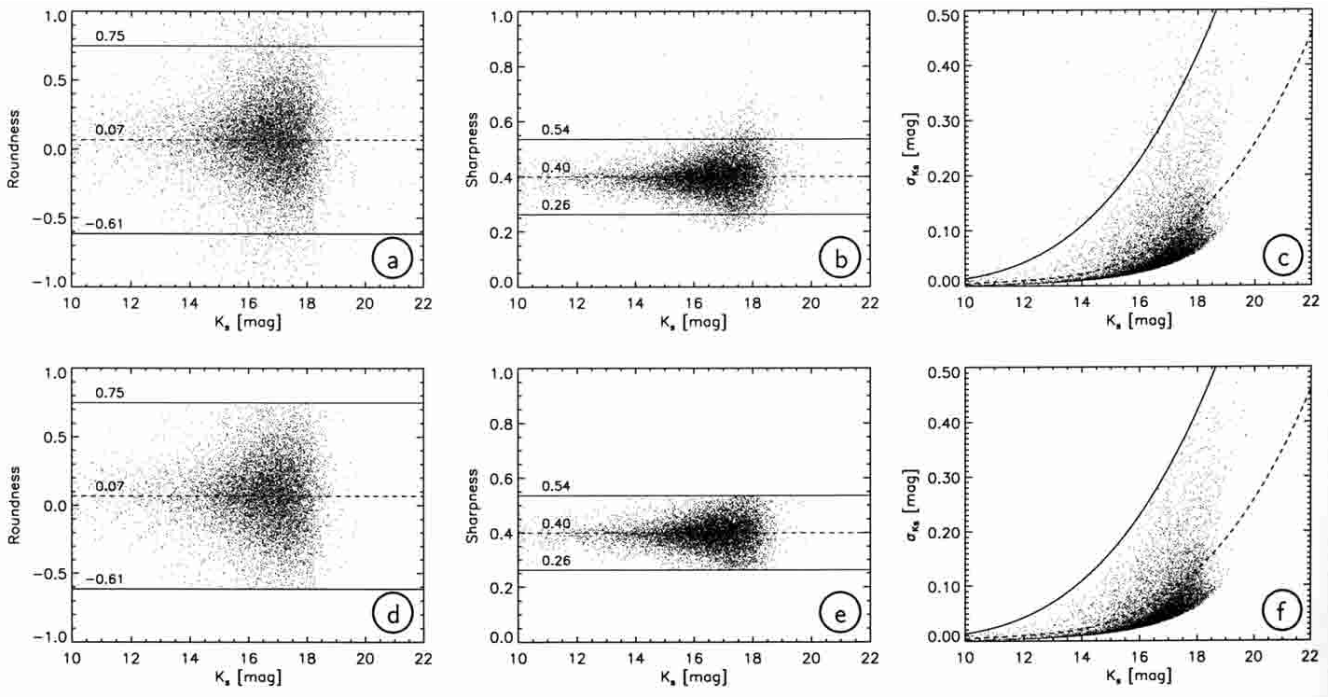

Fig. 2. Source selection based on parameters assigned by the DAOFIND and PHOT tasks using a 3 pixel aperture: roundness (left), sharpness (middle) and photometric error (right) versus K_s magnitude. While the upper panels display all stellar candidates, the lower panels show only those sources which fulfill the selection criteria. Dashed horizontal lines indicate mean values, solid lines mark $\pm 3\sigma$ deviations (panels **a)**, **b)**, **d)** and **e)**) and $+5\sigma$ deviations (panels **c)** and **f)**) from the corresponding mean value.

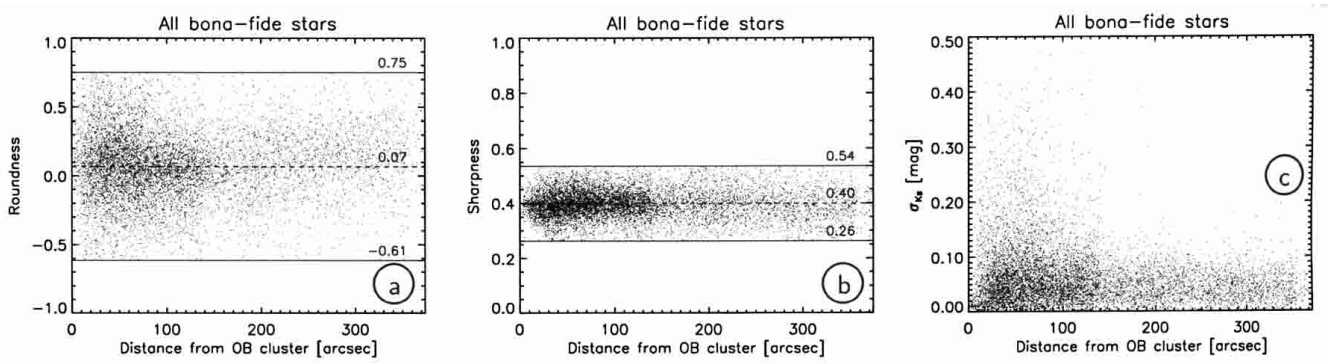

Fig. 3. Distribution of all selected sources, i.e. bona-fide stars (represented by their three selection parameters) versus distance from the center of the OB cluster.

of at least two images of one and the same star) spread all over the mosaic. Obviously, ISAAC is suffering from image distortion resulting in discrepancies of up to 4 pixels, i.e. about $0\farcs6$ (which is larger than the FWHM of the PSF) in the position of sources. Hence, before combining the individual frames, we applied a geometric transformation of all target frames using both spline3 interpolation and third order polynomial fitting.

After combining the corrected frames neither fake binary/multiple stars nor artificially elongated intensity profiles could be found any more. Nevertheless, in order to check the positions of stars, the K_s mosaic was registered and compared to an optical image obtained with the ESO / MPIA WFI on the 2.2 m telescope (Nürnberger 2002b). All over the mosaic, discrepancies in the peak position of stellar profiles were found to be less than a tenth of the PSF width. The final mosaic is presented in Fig. 1, and its corresponding effective integration time is given in the left panel of Fig. 4.

3. Source selection / rejection and photometry

In a first step, we determined the typical FWHM of the source profiles using the task IMEXAM within IRAF on about 200 bright, non-saturated and relatively isolated stars spread all over the K_s mosaic. We find that the

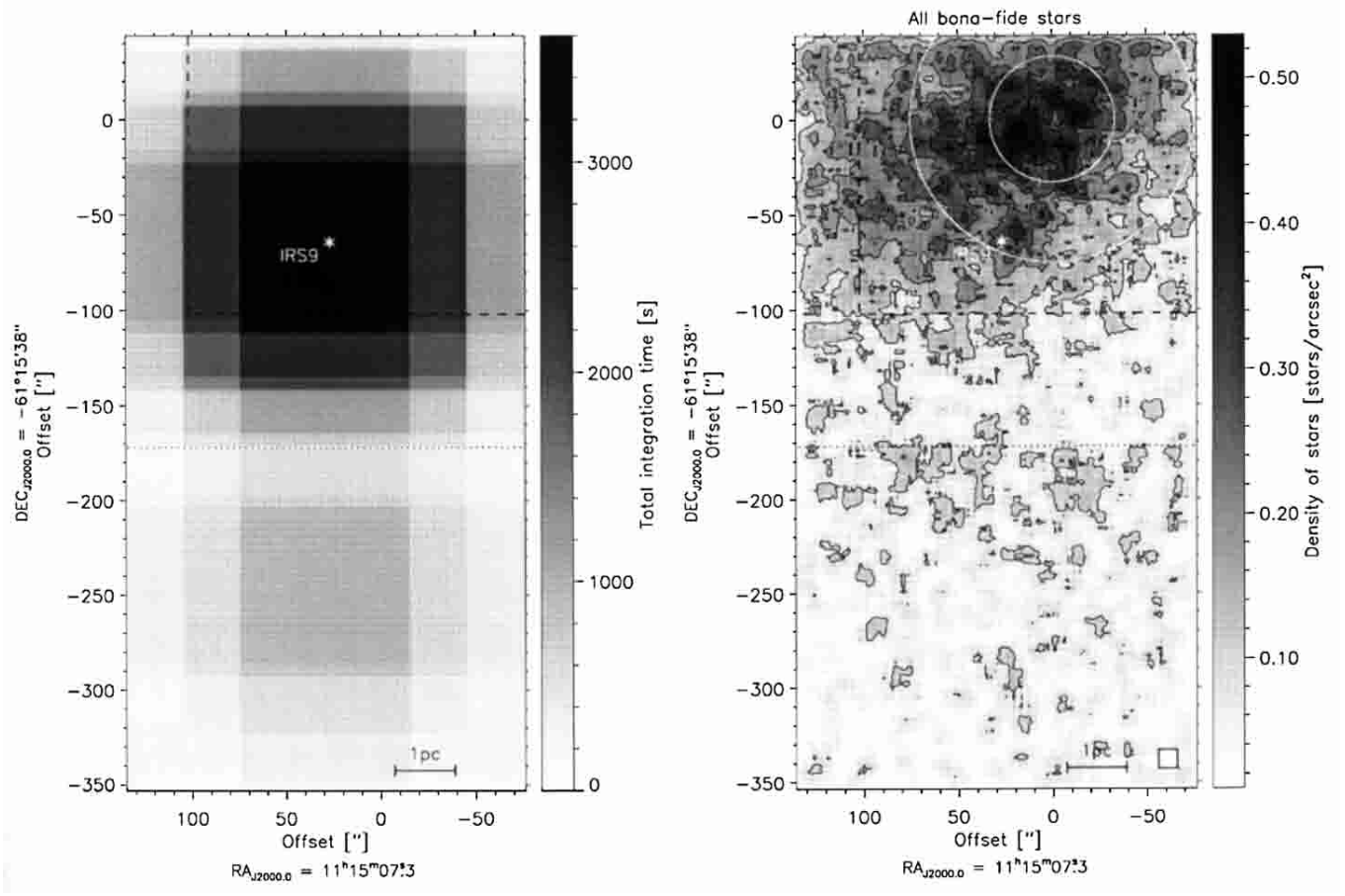

Fig. 4. Distribution of integration time over the observed field-of-view (left panel) directly compared to the surface density of all bona-fide stars (right panel). As in Fig. 1 the position of the infrared source IRS 9 is given by an asterisk. For illustration, the inner white circle indicates a radius of 33″ inside of which B+99 have performed their study of cluster stars. The outer white circle marks a radius of 75″ outside of which B+99 have derived their field star statistics. The square in the lower right corner of the right panel gives the aperture size used for the evaluation of the stellar surface density.

FWHM does not vary significantly over the whole mosaic and is on the order of 3 pixels (we measured $0\farcs45 \pm 0\farcs03$). Then, by setting the detection threshold 5σ above the background noise level the mosaic was searched for candidate stars with DAOFIND of the DAOPHOT package (Stetson 1987). Next we performed digital aperture photometry using PHOT with an aperture of radius 3 pixels – larger apertures increase the risk of flux contamination by nearby neighbouring sources – in order to derive instrumental magnitudes for all candidate stars. During the DAOFIND and PHOT procedures, three parameters were assigned to each source: the roundness, the sharpness and the photometric error. By considering their statistical scatter, these parameters were subsequently used to discriminate between stellar objects and noise peaks of diffraction spikes, saturated stars, hot pixels and/or diffuse elongated non-stellar structures.

We obtain the following mean values and standard deviations (averaged over the whole accessible magnitude range): 0.07 ± 0.23 for the roundness and 0.40 ± 0.05 for the sharpness (Fig. 2, panels a+b). Corresponding values of the photometric error were determined on $0\fm1$ wide bins (Fig. 2, panel c) and amount to $0\fm19 \pm 0\fm07$ for sources with $K_s \sim 19^m$. Taking these values into account, any object was excluded from the final list when either its roundness or its sharpness exceeded the mean value by more than $\pm 3\,\sigma$, or its photometric error exceeded the mean value by more than $+5\,\sigma$ (Fig. 2). The three criteria are complementary to each other with respect to source rejection. Careful inspection of rejected objects showed that in almost all cases they were indeed hot pixels or extended starless emission features. A significant fraction of rejected sources was located in the innermost 30″ of the OB cluster, where on the one hand the number of bright sources with saturated stellar profiles (or with digital counts lying in the non-linear range of the detector) is very high and on the other hand a reliable detection of faint sources is impossible due to the stellar crowding. About two dozen of the brightest and highly saturated stars (e.g. IRS 9) are not contained in our final list, which is therefore also incomplete for very bright stars. In the end, out of a total of 10 216 stellar candidates a sample of 8964 sources, i.e. bona-fide stars, was selected.

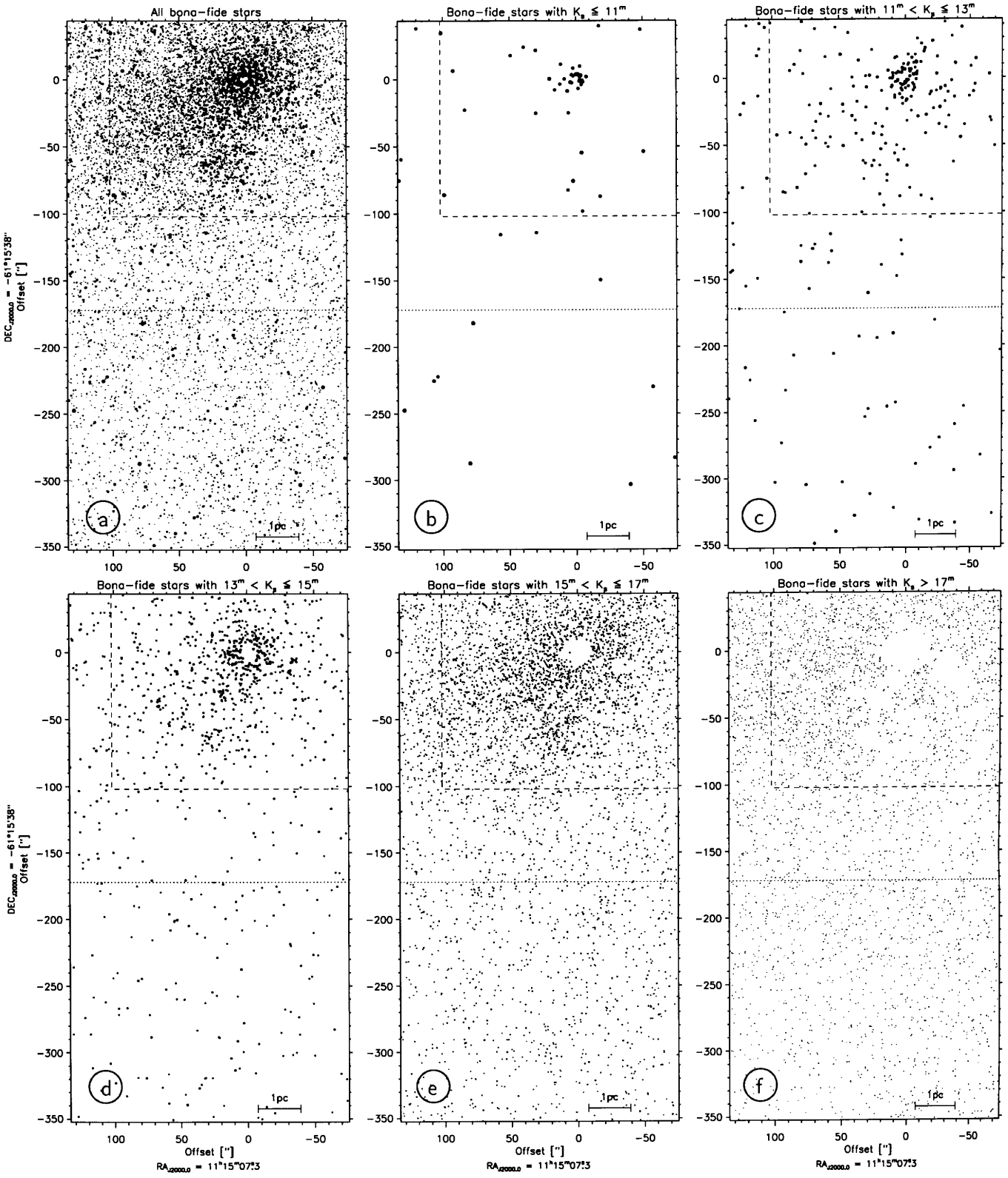

Fig. 5. The spatial distribution of bona-fide stars. While in panel a the whole sample is displayed, the other panels show the stars within (2^m wide) bins of K_s magnitude. In order to enhance the visibility of low luminosity sources, the magnitude scale is converted into a linear scale for the symbol sizes. Note by comparison with Fig. 1 that the brightest K_s sources (in total about two dozen; e.g. IRS 9) are not included, as they are saturated and thus do not match our selection criteria.

Photometric calibration for our aperture photometry was achieved by measuring the photometric zeropoint from observations of four different standard stars (FS 19, S279-F, S064-F, S791-C) and applying the

appropriate aperture correction. We estimate the typical uncertainty of our photometry – including uncertainties of the zeropoint and the aperture correction – to $\sigma_{Ks} \leq 0\overset{\mathrm{m}}{.}05$ ($11^{\mathrm{m}} < K_{\mathrm{s}} \leq 14^{\mathrm{m}}$), $\sigma_{Ks} \leq 0\overset{\mathrm{m}}{.}07$ ($14^{\mathrm{m}} < K_{\mathrm{s}} \leq 16^{\mathrm{m}}$) and $\sigma_{Ks} \leq 0\overset{\mathrm{m}}{.}10$ ($16^{\mathrm{m}} < K_{\mathrm{s}} \leq 17^{\mathrm{m}}$). Stars brighter than 11^{m} are close to the saturation limit, so that their photometry is affected by detector non-linearity. Limiting magnitudes ($5\,\sigma$ peak flux detections) are typically $19\overset{\mathrm{m}}{.}4$ for the non-crowded southern part of the mosaic, and $19\overset{\mathrm{m}}{.}1$ for the cluster and bright nebulous regions.

In Fig. 3 the distribution of bona-fide stars is plotted versus the distance from the center of the OB cluster. A relatively large number of stars is found within $150''$ of the cluster center. While roundness and sharpness show a very similar scatter at all radii, the scatter in photometric error is clearly larger for stars within $150''$ radius of the cluster center. This is due to the increased stellar crowding. Profile fitting, i.e. PSF fitting photometry would provide more accurate results for stars in the crowded cluster region. However, as the mosaic is composed of many individual images which do not or only partially overlap the PSF is, strictly speaking, physically *not* the same all over the mosaic. Furthermore, the results and conclusions presented here in this paper are not affected by the slightly larger photometric uncertainty in aperture photometry. In a forthcoming paper we will provide a complete catalog of stars with photometry derived from PSF fitting procedures performed on those 20 images having the best image quality. Again, we emphasize that results achieved from aperture photometry are fully consistent with those obtained via PSF photometry.

4. Completeness tests

Completeness limits were determined by adding artificial stars to the mosaic, then using DAOFIND with the same parameters as above to re-allocate them. Each test run comprised 100 artificial stars which were randomly spread all over the mosaic, but restricted in their magnitude to 1^{m} wide bins. For the same magnitude bin the procedure was repeated 10 times to obtain statistically significant counts, before we continued with the next magnitude bin. This way the magnitude range from 10^{m} to 20^{m} was covered. The total number of 10 000 artificial stars is roughly the same as the number of bona-fide stars detected in the mosaic and hence represents a statistically significant sample.

Based on these statistics we conclude that our star counts are basically complete ($> 90\%$) for the magnitude range 10^{m}–17^{m} all over the mosaic, except for the innermost $30''$ of the cluster. About 30% of the artificial stars are missed by DAOFIND when they are located at distances less than $30''$ from the cluster center, which must be attributed to the enormous stellar crowding in this area. The fact that almost all sources with $K_{\mathrm{s}} \leq 17^{\mathrm{m}}$ at radii $>30''$ are retrieved, independent of the amount of diffuse emission in their immediate vicinity, also proves our usage of a uniform selection criteria all over the mosaic to be in general a good choice, at least for the magnitude range 10^{m}–17^{m}.

Beyond 17^{m} the completeness of star counts significantly decreases and also varies with the amount of diffuse nebular emission. While for the 17^{m}–18^{m} bin still 85% (southern half of the mosaic, low nebulosity) and 75% (northern half of the mosaic, high nebulosity and stellar crowding) of the artificial stars are found, the count numbers drop to about 60% and 50% (low nebulosity and high nebulosity, respectively) for stars with magnitudes between 18^{m} and 20^{m}.

According to these test results we assume a completeness limit of $K_{\mathrm{s}} = 17^{\mathrm{m}}$ at radii $> 30''$ from the cluster center for our further interpretation of the data set.

5. Results and analysis

5.1. Spatial distribution of bona-fide stars

A synthetic map of all bona-fide stars is shown in Fig. 5a. Additionally, we present five maps for which the bona-fide stars were grouped in bins according to their K_{s} magnitude (Figs. 5b–f).

Although the most massive and most energetic cluster members of spectral type O and WR (see e.g. Melnick et al. 1989; Moffat et al. 1994; Drissen et al. 1995; Hofmann et al. 1995) are discarded from our sample due to saturation, the few luminous sources ($K_{\mathrm{s}} \leq 11^{\mathrm{m}}$; likely high mass main sequence stars if they are cluster members) found in panel b are clearly concentrated towards the center of the NGC 3603 cluster. In panels c and d the same clustering is seen for stars with $11^{\mathrm{m}} < K_{\mathrm{s}} \leq 15^{\mathrm{m}}$ (which are likely main sequence stars of high and intermediate mass if they are cluster members) as already noted by E+98. Low luminosity sources ($15^{\mathrm{m}} < K_{\mathrm{s}} \leq 17^{\mathrm{m}}$; see panel e) are apparently spread all over the northern half of the mosaic, but still with a slight tendency to cluster toward the OB cluster center. A significant fraction of them is located at radii much larger than $50''$. Beyond the completeness limit ($K_{\mathrm{s}} > 17^{\mathrm{m}}$; panel f) cluster stars seem to be spatially wide-spread, though their surface density is barely enhanced in comparison to the large number of field stars. However, this appearance of less pronounced clustering of faint sources is probably an effect of increasing incompleteness with decreasing radius from the cluster center.

It is obvious from panels d–f that a significant number of stars is missed towards the cluster center, which is more likely caused by the enormous stellar crowding and hence our inability to reliably detect weak sources than by any true deficiency of stars. This incompleteness is restricted to the innermost region ($r \lesssim 10''$) for the range $13^{\mathrm{m}} < K_{\mathrm{s}} \leq 15^{\mathrm{m}}$, but it affects a relatively large area (up to $r \sim 30''$) at fainter K_{s} magnitudes. One must keep this in mind when analyzing and interpreting (K_{s}-band) luminosity functions of the cluster center.

As can be seen in Fig. 5f, similar zones – which are apparently void of low luminosity sources – are associated

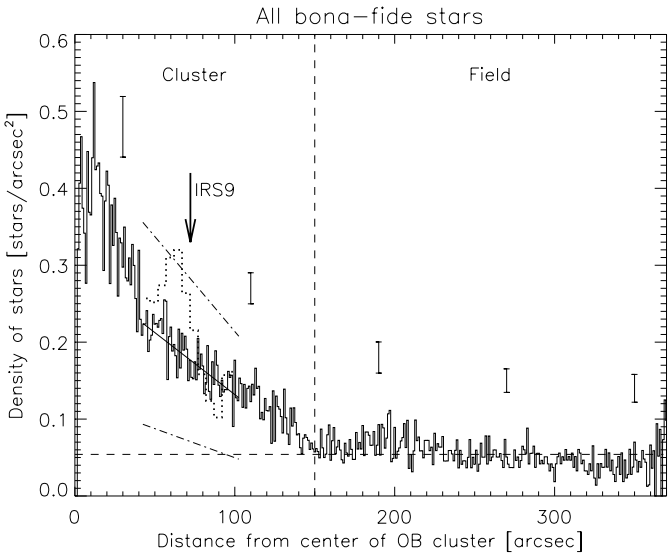

Fig. 6. The radial density distribution of all bona-fide stars. Typical error bars ($\pm\sqrt{N}$) are given for five distinct radii, and are offset for better visibility. The dashed horizontal line indicates the mean density of field stars, which was determined at radii between 180″ and 350″. The cluster radius at $\sim$150″ ± 15″ (see Fig. 7 and the text for its determination) is marked by the dashed vertical line. We also provide the position of IRS 9 and a separate statistics (dotted histogram) for 10° wide ring segments located within 5″ wide annuli towards IRS 9. For all the other 10° wide ring segments of the same annuli, mean values and $\pm1\sigma$ deviations were calculated (solid and dash-dotted straight lines, respectively).

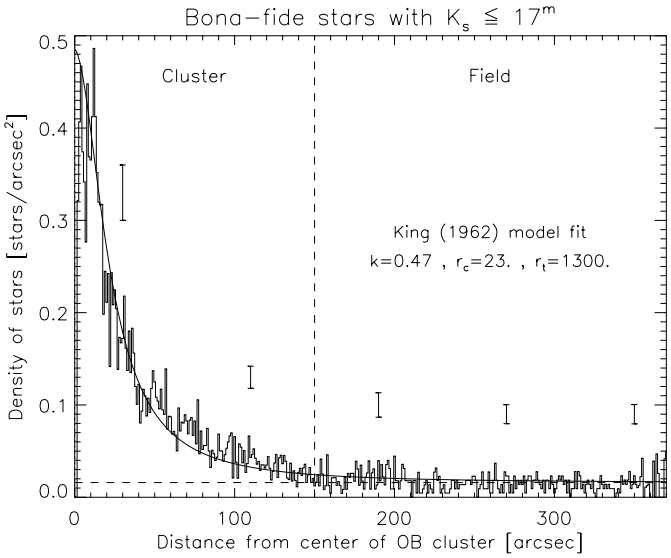

Fig. 7. The radial density distribution of bona-fide stars with $K_s \leq 17^m$ (complete sub-sample). The solid curve represents the best King model fit to the overall distribution (see the text for details). Like in Fig. 6, the dashed horizontal line indicates the mean density of field stars and the dashed vertical line at $\sim$150″ marks the cluster radius (given by the point at which the King model fit decreases below the $+3\sigma$ deviation from the mean field star density). It can be considered accurate to about ± 15″. The error bars give $\pm\sqrt{N}$ uncertainties.

with IRS 9 and the two prominent pillars. While the first might be due to the crowding of luminous IRS 9 sources, the latter two can be attributed to steep gradients and/or large inhomogenities in the diffuse emission of the pillars. This prevents a reliable photometry of K_s-band sources (i.e. causes their exclusion from our sample) which are definitely detected there. In that respect it is noteworthy that our statistics (for both cluster stars and field stars) are basically not affected by differential extinction. In all six panels of Fig. 5 we do not recognize any significant variation of star counts which might be correlated with the observed distribution of molecular gas shown in Fig. 1. This suggests two conclusions: First, the molecular clumps associated with NGC 3603 are much more compact than can be estimated from our CS (2–1) observations taken with a beam size of $\sim$50″. In fact, $C^{18}O$ (2–1) data at (by a factor of 2) higher angular resolution support this interpretation (see Fig. 1 of Nürnberger et al. 2002a). Second, the bulk of field stars lies in front of the cluster, as recently noted by Sagar et al. (2001). Such behaviour is also in full agreement with NGC 3603's location at the outer edge of the Carina arm and beyond its tangential point.

5.2. Surface density of bona-fide stars and cluster asymmetry

The stellar surface density distribution may be used to study any possible deviation of the NGC 3603 cluster from spherical symmetry. The right panel of Fig. 4 suggests that there exists an enhancement of stars towards the SE-E direction, while a deficiency of stars may be present towards the SW. In order to quantify a possible cluster elongation, we smoothed the observed surface density distribution with a circular Gaussian filter of width $\sigma = 3$ pixels and fitted elliptical isophotes to the smoothed distribution. The resulting ellipticity, defined as $e = 1 - (\,\text{minor axis} / \text{major axis}\,)$, is 0.29 ± 0.01 with a position angle of PA = 127° ± 2°. However, if we use only the complete sample the ellipticity is much less pronounced but still present, having $e = 0.22 \pm 0.01$ and PA = 133° ± 1°.

The cause for the observed elongation might be tidal interactions between the NGC 3603 cluster and either the Galactic Center or the nearby Carina arm, since the elongation is oriented almost parallel to the galactic plane. Alternatively, the cluster could have emerged from a non-spherical molecular cloud structure, which – as the cluster is very young – is still reflected in the currently observed stellar density distribution. CO and CS data (Nürnberger 2002a) do not provide evidence for a significant absorption effect, i.e. there is no correlation between the elongated shape of the cluster and the (non-)presence of molecular material in the foreground.

5.3. Radial density distribution of bona-fide stars

In Fig. 6 we plot the radial surface density distribution of all bona-fide stars covering distances up to 370″ from the

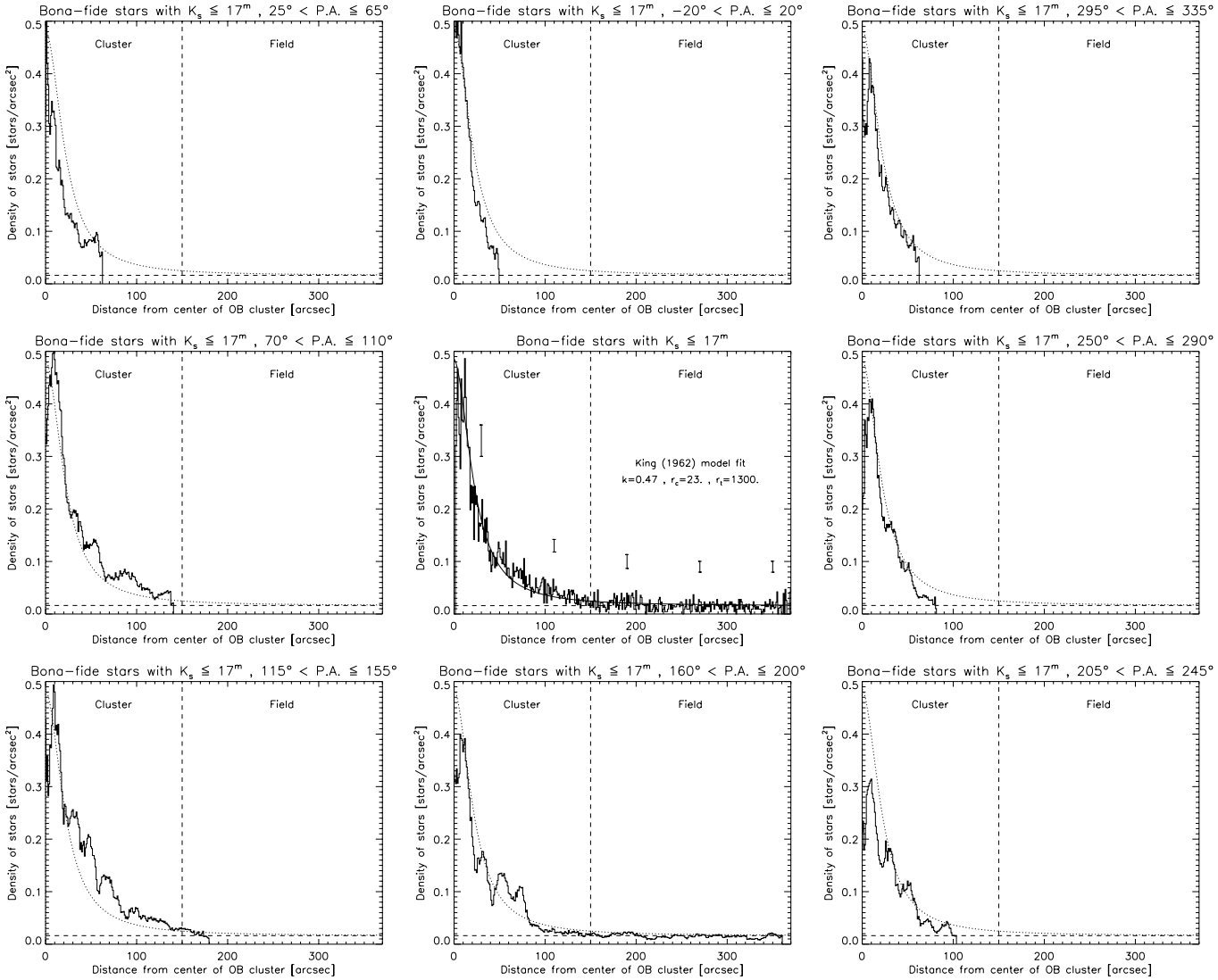

Fig. 8. The radial density distribution obtained for bona-fide stars within eight distinct angular segments. Rapid turnovers to zero are caused by reaching the borderline of the surveyed area. For the purpose of comparison, the central panel repeats the overall distribution already shown in Fig. 7, and the dotted curve in the outer panels is the same King profile as in the central panel.

center of the OB cluster, which is given by the mass center of the HD 97950 system (see Sect. 2 and Fig. 1). Star counts were computed for concentric rings of width 1″ and normalized to the area of each ring. The error bars shown are derived from simple Poisson statistics ($\pm\sqrt{N}$). Dashed horizontal and vertical lines indicate the mean density of field stars (0.054 ± 0.010 stars / arcsec^2) and the cluster radius (∼150″), respectively. The following sections give a short description of how these two parameters are derived.

5.3.1. King model fit

As the radial density distribution shown in Fig. 6 is expected to be affected by incompleteness, we consider for further analysis only the complete part of our sample, i.e. all bona-fide stars with $K_\mathrm{s} \leq 17^\mathrm{m}$. For these sources we compare in Fig. 7 the observed projected stellar density profile with a King model.

Usually, King models are successfully used to fit stellar surface density and / or surface brightness distributions of Globular Clusters, old galactic clusters as well as dwarf galaxies (e.g. King 1966; King et al. 1968; Djorgovsky & King 1986). The observed density profile of NGC 3603 was fitted with the empirical formula found by King (1962):

$$f(r) \;=\; k \cdot \left[\frac{1}{\sqrt{1+(r/r_\mathrm{c})^2}} \;-\; \frac{1}{\sqrt{1+(r_\mathrm{t}/r_\mathrm{c})^2}} \right]^2$$

where $f(r)$ gives the density distribution of stars in projection in dependence on the distance r from the cluster center. The parameter k is a normalisation related to the total number of stars in the cluster center, r_c is the core

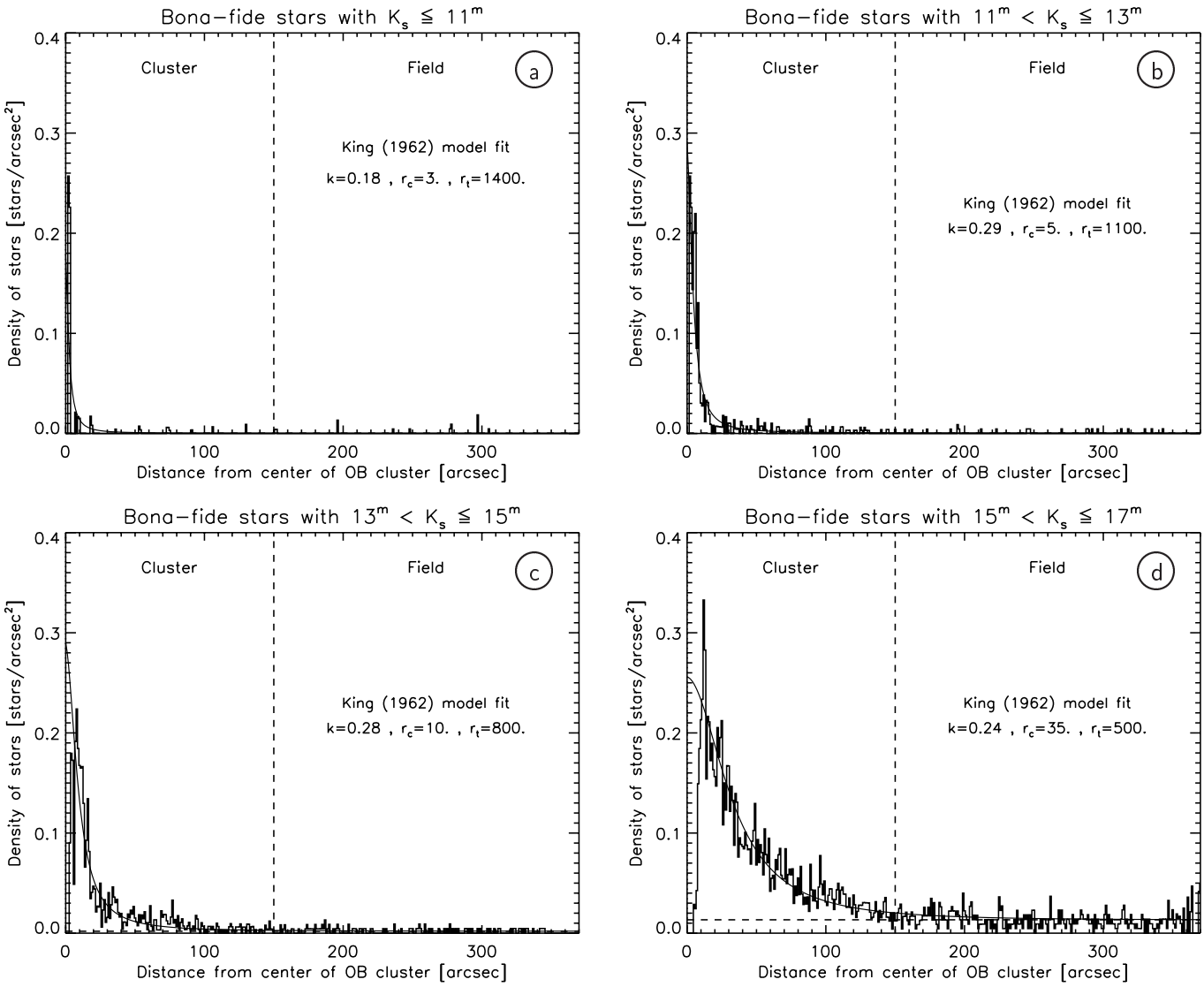

Fig. 9. The radial density distribution of bona-fide stars lying within the completeness limit of our study (which is $K_{\rm s} \sim 17^{\rm m}$), separated into the same four magnitude bins as already used for panels **b)**–**e)** of Fig. 5. For each magnitude range the best King profile fit and the corresponding parameter set is given.

radius (also called the King radius) which essentially determines how strongly peaked the density distribution is, and $r_{\rm t}$ is the tidal radius where $f(r)$ approaches zero.

The best King model fit to the overall distribution is shown as a solid line in Fig. 7 and was obtained with the following parameter set: $k = 0.47$ stars/arcsec^2, $r_{\rm c} = 23''$ (0.78 pc) and $r_{\rm t} = 1300''$ (44 pc). The procedure used a non-linear least square fitting following the Levenberg-Marquardt method (Press et al. 1989) and turned out to be sensitive to the core radius but rather insensitive to the other two parameters. Concerning $r_{\rm t}$, it is generally difficult to constrain the tidal radius from the stellar density profile (e.g. Kaluzny & Udalski 1992). Furthermore, in our case, the normalisation parameter k barely provides any additional information because of incomplete star counts (due to stellar crowding) for radii smaller than $30''$. Hence, the uncertainties of the found solution are $\sigma_{\rm k} = \pm 0.05$ stars/arcsec^2, $\sigma_{r_{\rm c}} = \pm 5''$ and $\sigma_{r_{\rm t}} = \pm 200''$.

We have also checked, if the slight ellipticity of the cluster does effect the result of the King model fit: In Fig. 8 we plot the radial density distribution of bona-fide stars for 40° wide angular segments at eight distinct position angles and compare them with the overall density distribution (center panel). In agreement with Fig. 4 (right panel; see also Sect. 5.2) we notice a slight enhancement of stars towards the SE-E of the cluster center. Apart from this, there are no significant deviations of the radial density distributions at different position angles from the overall profile. Thus we conclude that the ellipticity does not affect the results of our King model fit.

Similar to Figs. 6 and 7, E+98 show a plot of the projected stellar density for the NGC 3603 cluster, but limited to the core region ($r \leq 40''$). While their

absolute observed numbers of stars per square-arcseconds at $r = 30''$–$40''$ agree quite well with our values, their profile fitting yields a core radius of $r_c = 13''$ (0.44 pc), much smaller than the value derived from our observations. The difference is mainly due to two facts: First, our number counts for radii smaller than $30''$ are underestimated due to incompleteness caused by the very high stellar density in the cluster center. Second, our study traces primarily the intermediate and low mass stars, the most massive stars of spectral type O are excluded due to saturation. Therefore, the resulting core radius of $r_c = 23'' \pm 5''$ should be regarded as an upper limit.

As shown in Fig. 9, where we separate the complete subsample into four magnitude bins equal to those used in panels b–e of Fig. 5, the core radius is also highly dependent on the investigated magnitude range (i.e. mass range): $r_c \sim 3''$ (0.1 pc) for stars with $K_s \leq 11^m$ (likely high mass main sequence stars; panel a), $r_c \sim 5''$–$10''$ (0.2–0.3 pc) for stars with $11^m < K_s \leq 15^m$ (main sequence stars of high and intermediate mass; panels b and c) and $r_c \sim 35''$ (1.2 pc) for stars with $15^m < K_s \leq 17^m$ (mostly low mass pre-main sequence stars; panel d). Obviously, the more massive stars are more concentrated towards the center of the NGC 3603 cluster. A similar behaviour has been found for R 136 by Brandl et al. (1996; see their Figs. 15 and 16).

Finally, we wish to note that it is very interesting that a stellar cluster as young as the NGC 3603 cluster can be well fitted with a King profile, because King models describe solutions for stellar systems in dynamical equilibrium. Clearly, since important physical parameters – such as stellar kinematic information (i.e. velocity dispersion) or the total stellar mass of the NGC 3603 cluster – is lacking, we cannot evaluate the cluster's dynamical status. Nevertheless, it is possible to carry out some order of magnitude estimations. Let us assume a velocity dispersion of $\sigma \sim 7\,\mathrm{km\,s^{-1}}$, a typical average value for globular clusters (Meylan & Pryor 1993). Then the cluster crossing time $t_{\mathrm{cross}} \approx 2r/\sigma$ (where r is the cluster radius; see Sect. 5.3.2) for the NGC 3603 OB cluster is 1.4 Myr, which is on the order of the age of the cluster. Hence, the cluster should still be largely unaffected by standard relaxation processes that would bring the cluster close to an equilibrium state. Only for its central 0.5 pc relaxation via two-body encounters may have played some role, since crossing times are significantly shorter.

Also the very young Orion Nebula Cluster shows a radial stellar profile that is in accordance with a King profile (Hillenbrand & Hartmann 1998). Since both clusters, the NGC 3603 cluster as well as the Orion Nebula Cluster, are too young to have experienced significant two-body relaxation, the structural similarity with globular clusters and older Galactic clusters is striking. This suggests that some very basic dynamical process must regularize the structural appearance of clusters. Proposed processes include initial mixing and/or violent relaxation, or alternatively, the formation of stellar structures close to an equilibrium distribution.

5.3.2. Cluster radius

We can now use the observed radial profile from Fig. 7 to estimate the radius of the NGC 3603 OB cluster. Using the point at which the King model fit decreases below the $+3\,\sigma$ deviation from the mean field star density (determined from radii between $180''$ and $350''$) as a quantitative criterium, we derive a cluster radius of $150'' \pm 15''$ (marked by the dashed vertical line in Figs. 6 and 7). Assuming a distance of 7 kpc for NGC 3603, this corresponds to a linear radius of about 5 pc which is larger by a factor of 2.5 than the value assumed so far (Melnick et al. 1989).

This difference is not surprising as Melnick et al. could only use optically bright stars which are more concentrated towards the cluster center, as already discussed in Sect. 5.3.1, while the low luminosity stars are much more wide spread. In particular, comparison of Fig. 9d to Fig. 7 reveals that the large number of low luminosity stars dominates the overall density distribution of cluster stars and sets the cluster radius.

5.3.3. The infrared source IRS 9

In Fig. 6 we have also indicated the distance of IRS 9 from the cluster center. Separate statistics (dotted histogram) were calculated for 10° wide ring segments of $5''$ wide annuli, which cover the immediate environment of IRS 9. For all the other 10° wide ring segments of the same annuli mean values and 1σ deviations were calculated (solid and dash-dotted straight lines, respectively). The coarse binning to segments of 10° causes the angular variations of the stellar density to appear rather large. However, this reflects the slightly elliptical shape of the cluster as well as the small scale fluctuations of the stellar density (as already mentioned in Sect. 5).

Inwards of IRS 9 (at $r \sim 60''$) there seems to be a local enhancement of stellar density, while stars seem to be slightly deficient just outwards (at $r \sim 90''$). Certainly, this behaviour is statistically not significant ($+1.1\,\sigma$ and $-0.5\,\sigma$, respectively). But it is interesting to note as it might correlate with IRS 9 being located on the OB cluster facing side of an adjacent molecular cloud core (A_V up to 30^m) and having been blown free from its natal molecular environment by strong stellar winds, which originate from the O and WR stars of the main cluster. Such a scenario is consistent with a wind-blown cavity, centered on the OB cluster and mostly void of interstellar gas and dust (Balick et al. 1980; Clayton 1986, 1990), as well as with shape and orientation of two prominent pillars (Brandner et al. 2000).

Furthermore, IRS 9 features several near-infrared excess sources (Tapia et al. 2001) as well as at least three strong mid infrared emitters, which indicates that – although revealed from most of the interstellar material – these sources must still be deeply enshrouded in massive circumstellar envelopes of gas and dust (Nürnberger et al. 2002a; Nürnberger 2002b). The recent detection of IRS 9's brightest K_s-band source at radio and X-ray wavelengths

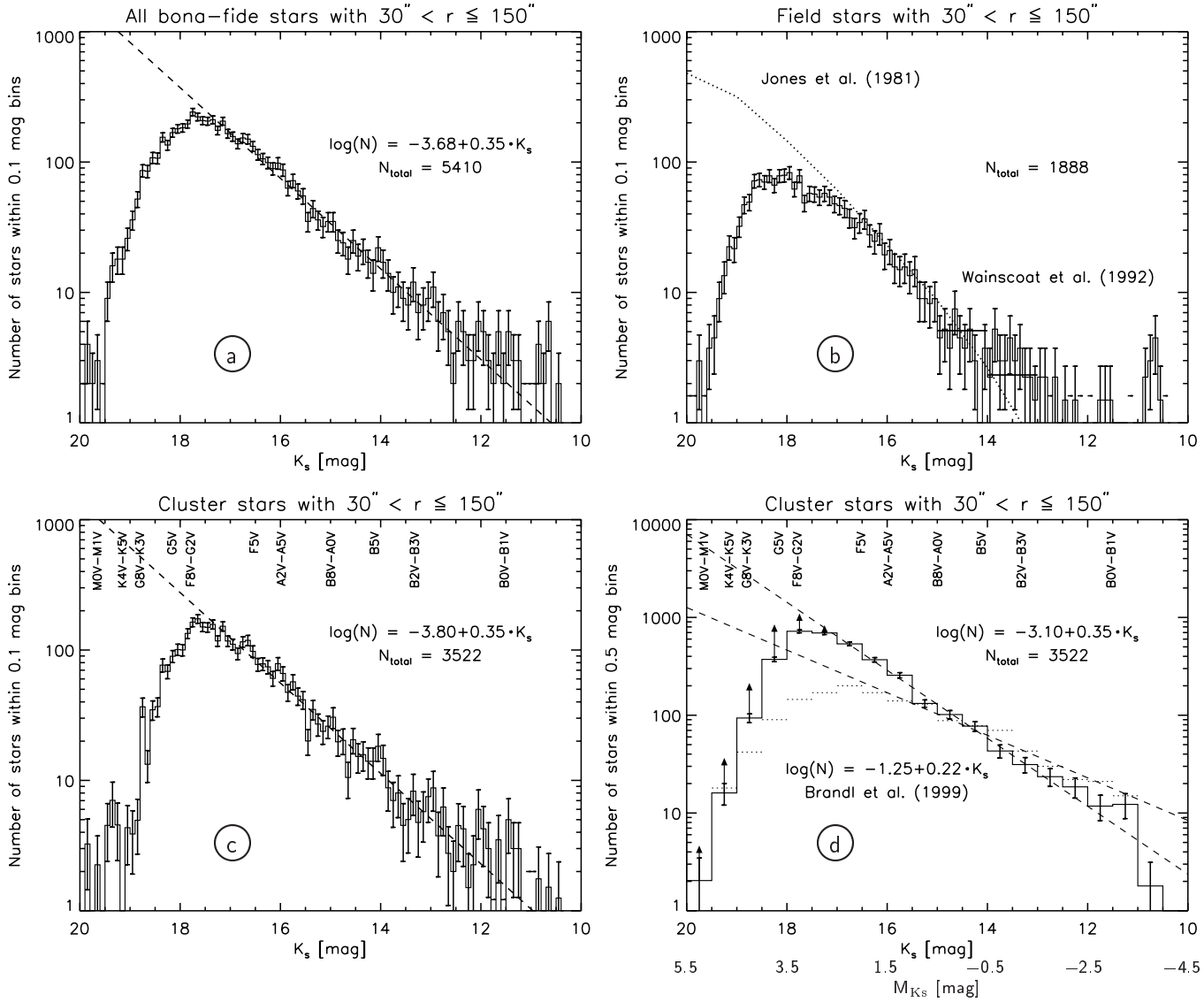

Fig. 10. K_s-band luminosity function obtained for all bona-fide stars lying within the range $30'' < r \leq 150''$. Panel **a)** comprises both cluster stars and field stars, while the two groups are separated in panels **b)** and **c)**. The distribution of field stars is compared to the expected one according to the galactic disk models of Jones et al. (1981; dotted curve) and Wainscoat et al. (1992; bold horizontal bars). In panel d the field star subtracted KLF of cluster stars is displayed again using $0\overset{\mathrm{m}}{.}5$ wide bins instead of $0\overset{\mathrm{m}}{.}1$ wide ones, which allows direct comparison with the results of B+99 ($r \leq 33''$; dotted histogram). Best fitting results for the KLFs of intermediate luminosity stars ($13^{\mathrm{m}} \lesssim K_{\mathrm{s}} \lesssim 16^{\mathrm{m}}$) are indicated by dashed lines. For bins longward of $K_{\mathrm{s}} = 17^{\mathrm{m}}$ arrows give a lower limit for the incompleteness correction of our sample, which is complete for $K_{\mathrm{s}} \leq 17^{\mathrm{m}}$. Assuming a lower limit of 6.3 kpc for the distance of NGC 3603 and a typical interstellar extinction of $A_V = 4\overset{\mathrm{m}}{.}5$ apparent magnitudes of stars convert into absolute magnitudes and corresponding spectral types of main sequence stars as annotated.

(Mücke et al. 2002 and Mücke, priv. comm., respectively) confirms this picture.

Hence, even if IRS 9 might barely stand out from the average density distribution of cluster stars, sources associated with IRS 9 most likely are in relatively early evolutionary stages when compared to the population of the NGC 3603 OB cluster. Therefore, IRS 9 might count as a sparse association of protostars in its own right (see the discussion in Nürnberger et al. 2002a and Nürnberger 2002b for more details).

5.4. K_s-band luminosity function

Near-infrared luminosity functions are a powerful tool to investigate emergent and initial mass functions (EMF and IMF, respectively; Meyer et al. 2000). Hence, during the last decade several studies have focused on determination and discussion of luminosity functions of young clusters (e.g. Lada et al. 1991, 1993a; Carpenter et al. 1993, 1997; Megeath et al. 1996; Hillenbrand 1997; Sirianni et al. 2000). However, although star formation in clusters occurs on short times-scales (i.e. in only one or two crossing

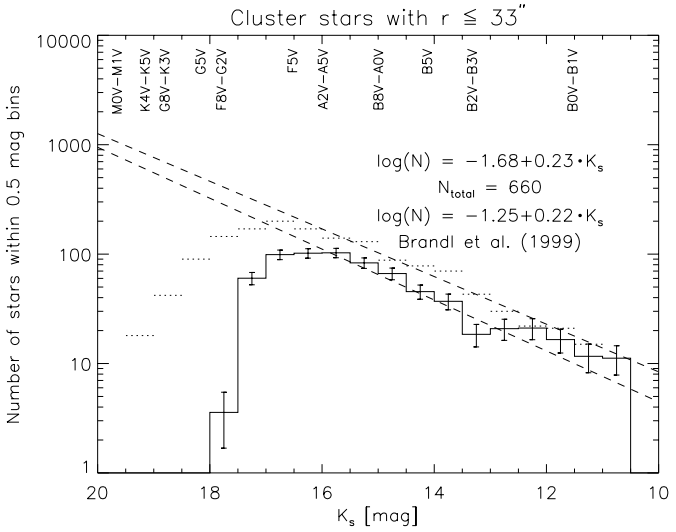

Fig. 11. K_s-band luminosity function for cluster stars with $r \leq 33''$ after subtraction of a "field star population" which was derived from the annulus $75'' < r \leq 102''$ (following Brandl et al. 1999).

times; Elmegreen 2000; Elmegreen et al. 2000), relatively large uncertainties in the most crucial parameters like the mass-luminosity relation and the stellar ages make it often difficult to interpret near-infrared luminosity functions in terms of the underlying mass function.

Young starburst clusters provide a scenario in which most of the stars are supposed to be formed (nearly) coeval. Thus, age determination for a relatively small number of cluster members allows to eliminate the stellar age as a free parameter in modeling the stellar mass function. In the case of the NGC 3603 OB cluster, recent studies by E+98 and B+99 have shown a relatively small spread of stellar ages. Stars with less than $4\,\mathcal{M}_\odot$ appear to be slightly younger (<1 Myr) than the more massive stars (2 . . . 3 Myr). However, the debate on the ages of both low mass and high mass cluster members is still open (see e.g. the discussions presented in E+98 and Crowther & Dessart 1998). In particular, taking into account the uncertainties of current stellar evolutionary models one might even speculate that low mass and high mass stars of the NGC 3603 cluster are coeval.

5.4.1. The observed KLF

Based on our VLT / ISAAC data, the overall K_s-band luminosity function of the NGC 3603 starburst cluster is presented in Fig. 10. Panel a gives the observed KLF of all bona-fide stars with radii between $30''$ and $150''$, i.e. it comprises both cluster and field stars. After appropriate subtraction of field stars – their KLF is displayed in panel b and discussed in Sect. 5.4.2 – we obtain the pure statistics of cluster stars (panel c).

The same KLF of cluster stars is shown again in panel d, using $0\overset{\mathrm{m}}{.}5$ wide bins instead of $0\overset{\mathrm{m}}{.}1$ wide ones in order to match the uncertainties of the photometric calibration of the weakest sources and to allow direct comparison with the results of B+99 (dotted histogram). For magnitude bins longward of $K_s = 17^{\mathrm{m}}$ arrows indicate a lower limit for the incompleteness correction of our sample, which is complete for $K_s < 17^{\mathrm{m}}$ over the range $30'' \leq r \leq 150''$.

In order to look for radial trends we have also extracted KLFs for five distinct annuli covering ranges from $r \leq 30''$ to $120'' < r \leq 150''$. These results are presented in Fig. 12 and can be directly compared to Fig. 10, as for each annulus the corresponding KLF of bona-fide stars (left column), field stars (middle column) and cluster stars (right column) is provided.

Taking into account a distance modulus of 14^{m} (i.e. a lower limit of 6.3 kpc for the distance of NGC 3603) as well as a foreground extinction of $A_V = 4\overset{\mathrm{m}}{.}5$, our apparent magnitudes convert into absolute magnitudes as annotated along the lower abscissa of Figs. 10d and 12c5. Based on the KLF parameters provided by Jones et al. (1981; their Table 2) we made an attempt to translate these magnitudes into spectral types by simplifying that all NGC 3603 cluster stars belong to luminosity class V. The corresponding spectral types are marked along the upper abscissa. Sources that are still in the pre-main sequence phase, however, are typically more luminous than on the main sequence and corresponding spectral types would shift to the right in our figures. For instance, assuming an age of 1 Myr for the NGC 3603 OB cluster and using the stellar evolutionary models by Baraffe et al. (1998), a star of $0.5\,\mathcal{M}_\odot$ will have $K_s \sim 17^{\mathrm{m}}$.

5.4.2. The field star KLF

The determination and subtraction of field star statistics is required for an analysis and interpretation of the luminosity function. Therefore, as the NGC 3603 OB cluster spreads out to radii of about $150''$ (see Sect. 5.3.2), we determine the statistics and the KLF of field stars at radii larger than $150''$, i.e. the southern half of our survey area is used for this purpose.

In order to check the reliability of the obtained field star KLF, we compare it to that expected from the Galactic disk models of Jones et al. (1981; dotted curve) and Wainscoat et al. (1992; bold horizontal bars) in panel b of Fig. 10 as well as in panels b1–b5 of Fig. 12. Both models comprise geometrically and physically realistic representations of infrared sources within the Galaxy and are complementary to each other in terms of the K_s-band magnitude range. While Wainscoat et al. (1992; see their Table 8) already list a KLF for the Galactic coordinates $l = 330°$ and $b = 0°$ (which are close to those of NGC 3603), we have used the Jones et al. (1981) model to calculate the total number of field stars per magnitude bin towards the exact coordinates of NGC 3603 ($l \sim 291\overset{\circ}{.}6$, $b \sim -0\overset{\circ}{.}5$). For this purpose we took into account

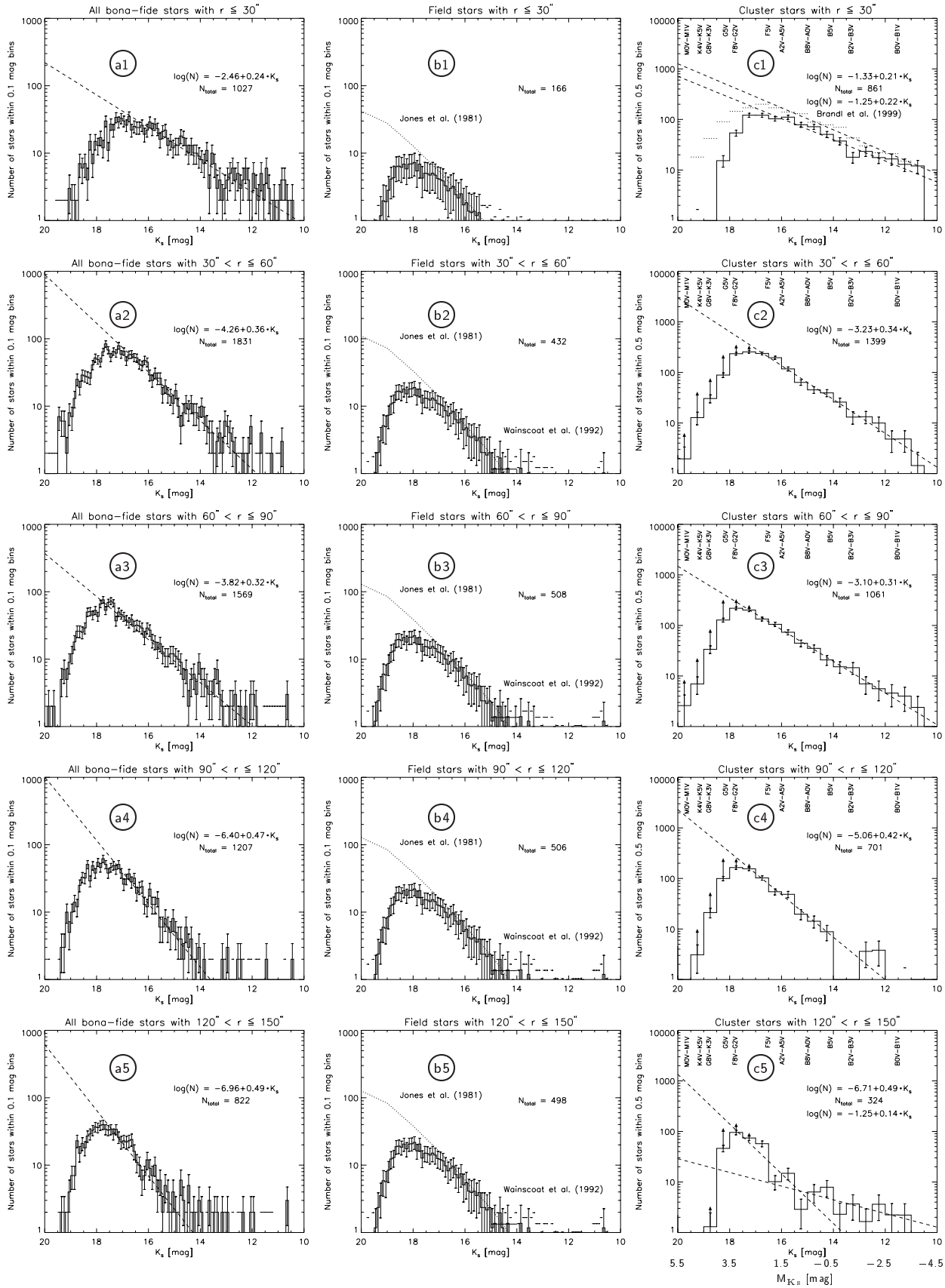

Fig. 12. K_s-band luminosity functions derived for five distinct annuli covering ranges from $r \leq 30''$ (top) to $120'' < r \leq 150''$ (bottom). The observed KLFs (which include both cluster stars and field stars) are found in the left column. In all cases field star statistics were obtained at radii $>150''$ and normalized to the actually observed area of each individual annulus (middle column). After field star subtraction the emergent cluster KLFs (binned to $0\overset{\mathrm{m}}{.}5$ wide units) are shown in the right column.

adequate populations of field stars in the distance range from 0.5 kpc to 14 kpc. The model results are in excellent agreement with our observed KLF of field stars for the range $11^{\rm m} \leq K_{\rm s} \leq 17^{\rm m}$ (the normalized values of Wainscoat et al. 1992 for the bins $11^{\rm m}$–$12^{\rm m}$ and $12^{\rm m}$–$13^{\rm m}$ lie just outside the ordinate range).

5.4.3. The cluster star KLF

With appropriate field star statistics at hand, we disentangle the count statistics of cluster stars from those of field stars at radii $\leq 150''$ and analyze the pure cluster KLF. This is done in several steps, considering different regions within the cluster.

First, we directly compare our data to the KLF presented by B+99. These authors derive a luminosity function for the innermost $33''$ of the NGC 3603 OB cluster, which is shown in Fig. 11. Following the same procedure as the one used by B+99, i.e. constructing the KLF for cluster stars with $r \leq 33''$ and subtracting a "field star population" derived from the annulus $75'' < r \leq 102''$, we obtain a KLF from our VLT data that is also plotted in Fig. 11. The comparison shows that our result does very well reproduce the relatively flat KLF slope for $K_{\rm s} < 16^{\rm m}$ reported by B+99. However, the two curves also reveal significant discrepancies in number counts, in particular for $K_{\rm s} > 16^{\rm m}$, which may be due to various reasons. E.g., the data set of B+99 was obtained under slightly better seeing conditions and with slightly larger total integration time (on the cluster center), which primarily explains the diverging results at the faint luminosity end. Also, the two samples have been derived from different selection / rejection procedures.

The flat slope of the KLFs in Fig. 11, however, is suspicious because it would be typical for a cluster consisting solely of main sequence stars (see the next but one paragraph), which contradicts the findings of B+99 that the low mass stars of NGC 3603 are still in a pre-main sequence evolutionary phase. A steeper slope is expected considering the large numbers of low mass pre-main sequence stars identified by B+99 (see their Fig. 2c). Could the flat slope be due to the subtraction of a "field star population" derived from $75'' < r \leq 102''$, which apparently is within the cluster region since the cluster extends to $r \approx 150''$?

In order to clarify this, we plot the KLF for the cluster center again in Fig. 12 c1, but this time with field star statistics derived from radii larger than $150''$ (i.e. the revised cluster radius was taken into account). In general, our result and that of B+99 are again in good agreement. Most interestingly, the resulting KLF slope is still very flat, consistent with those shown in Fig. 11. Hence we can rule out that the slope obtained by B+99 is affected by their choice of field star subtraction. Since we know from Sect. 4 that – at least for our data set – statistics of NGC 3603 cluster members (in particular of low luminosity sources) obtained at radii $<30''$ are highly incomplete, we believe that the flat slope is caused by this incompleteness and thus not representative for the real KLF of the cluster/cluster center. Expecting large uncertainties due to the enormous crowding of stars within the cluster center, we made no attempt to determine incompleteness corrections for the individual magnitude bins of Figs. 11 and 12 c1 .

A much better approach is to study the cluster KLF emerging from (complete) number counts in the range $30'' < r \leq 150''$ (Fig. 10). Panels c+d of Fig. 10 display the field star subtracted KLF of cluster stars, with the best power-law fit for the KLF of intermediate luminosity stars ($13^{\rm m} \lesssim K_{\rm s} \lesssim 16^{\rm m}$) indicated by a dashed line. In comparison to the results for the central cluster region and to the results of B+99 we obtain a much steeper cluster KLF, with a slope of about 0.35 ± 0.02 (independent of the magnitude binning). Assuming an average age of 1 Myr for the cluster stars (see the detailed discussion in E+98 and Crowther & Dessart 1998) and thus using the mass-luminosity relation $L_K \propto \mathcal{M}^{\beta}$ with $\beta \sim 1$ for low mass pre-main sequence stars (Lada et al. 1993b), one would expect values like $\alpha = \gamma \,/\, (\,2.5\,\beta\,) = 0.68$ and 0.54 for power-law IMFs with slopes $\gamma = 1.7$ (Miller-Scalo 1979; Scalo 1986) and 1.35 (Salpeter 1955), respectively. Increasing the mass-luminosity relation to $\beta \sim 2$ (in order to account for both the intermediate / high mass main sequence stars and the low mass pre-main sequence stars; Lada et al. 1993b) should result in KLF slopes of $\alpha = 0.27$ for a Salpeter type IMF and $\alpha = 0.34$ for a Miller-Scalo type IMF, which (i.e. the latter value) is obviously in very good agreement with our fit result.

In full agreement with the results of E+98 we do not find any turnover in the luminosity function down to solar-type stars, and probably not even down to sub-solar masses ($K_{\rm s} \sim 17^{\rm m}$–$18^{\rm m}$). Hence, the apparent turnover at $K_{\rm s} \sim 16\overset{\rm m}{.}5$ seen by B+99 must be an observational artifact due to incompleteness which they have presumed in their paper already. Given the fact that our statistics for both field stars and cluster stars show a turnover at $K_{\rm s} \sim 18^{\rm m}$ we believe that this is an observational artifact too. At the high luminosity end ($K_{\rm s} \leq 13^{\rm m}$) the cluster KLF apparently flattens ($\alpha \leq 0.2$; see Figs. 10d and 12c1), which would be consistent with a Salpeter type IMF for NGC 3603's massive stars which are already on the main sequence.

From panels c2–c5 of Fig. 12 we find some evidence for a steepening in the KLF with distance from the cluster center: $\alpha \sim 0.31 \ldots 0.34$ for the range $30'' < r \leq 90''$ and $\alpha \sim 0.42 \ldots 0.49$ for the range $90'' < r \leq 150''$. If confirmed this may be indicative for mass segregation within the cluster at a relatively early evolutionary stage ($\sim$1 Myr), either as a result of initial conditions (massive stars are born in the center) or as a result of rapid cluster evolution. Given the uncertainty ($\pm 15''$) for the cluster radius, which is half of the bin widths used here, the somewhat shallower KLF slope ($\alpha \sim 0.14$) seen in panel c5 for the magnitude range $16^{\rm m} \gtrsim K_{\rm s} \gtrsim 11^{\rm m}$ might be caused by a remnant, non-negligible contamination with field stars.

6. Summary

We have presented results from deep K_s-band observations of NGC 3603, taking advantage of the capabilities (high angular resolution and high sensitivity) offered by ISAAC at ESO's VLT Antu. We were able to set new constraints on radius and KLF of the NGC 3603 starburst cluster. In particular, we find the following:

- Although the highly crowded cluster center ($r < 30''$) needs to be treated carefully, the overall radial stellar density distribution is successfully fit by a King profile with a core radius of $r_c = 23'' \pm 5''$ (corresponding to $0.78\,\mathrm{pc} \pm 0.17\,\mathrm{pc}$ at a distance of 7 kpc). The core radius is highly dependent on the investigated range of K_s magnitudes, which suggests that the more massive stars are obviously more concentrated towards the cluster center.
- The cluster spreads out to radii of the order $150''$ (i.e. about 5 pc). This is larger by a factor of 2.5 than the value assumed so far (Melnick et al. 1989).
- The cluster radius is determined by the low mass stars. Thus, underestimating the cluster radius converts primarily into an underestimation of the low mass cluster population.
- For cluster radii larger than $30''$ we find a gradual steepening of the cluster KLF which might be interpreted as an evidence for mass segregation, either initial or dynamical.
- The KLF of NGC 3603 shows no turnover for $K_s \lesssim 17^m$, which corresponds to $\mathcal{M} \gtrsim 0.5\,\mathcal{M}_\odot$ for 1 Myr old cluster members. Taking into account an appropriate correction for incompleteness the KLF probably rises even in the range $K_s \sim 17^m$–18^m.
- In contrast to the flat KLF determined for the incomplete star counts at cluster radii $<30''$, for radii between $30''$ and $150''$ we obtain a much steeper KLF, with a slope of 0.35 ± 0.02 for the range of intermediate luminosity stars. This is consistent with a Miller-Scalo type IMF of a 1 Myr old stellar cluster if one assumes a power-law index of 2 for the mass-luminosity relation of both intermediate mass main sequence stars and low mass pre-main sequence stars. At the high luminosity end the observed KLF probably flattens (slope $\sim$0.2), in agreement with a Salpeter type IMF for NGC 3603's massive stars which are also on the main sequence.

Acknowledgements. It is a great pleasure to express our gratitude to the Paranal Science Operations team for conducting the observations in service mode. We thank Michael Geffert for comments and discussions on an early version of the manuscript and the referee Bernhard Brandl for helpful suggestions. This research has been supported by the Deutsche Forschungsgemeinschaft (DFG) in the framework of its "Physics of Star Formation" program under grants Yo 5/23-1 and Zi 242/22-2. DEAN also acknowledges support by IRAM, Grenoble.

References

Balick, B., Boeshaar, G. O., & Gull, T. R. 1980, ApJ, 242, 584
Baraffe, I., Chabrier, G., Allard, F., & Hauschildt, P. H. 1998, A&A, 337, 403
Brandl, B., Sams, B. J., Bertoldi, F., et al. 1996, ApJ, 466, 254
Brandl, B., Brandner, W., Eisenhauer, F., et al. 1999, A&A, 352, L69 (B+99)
Brandner, W., Grebel, E. K., Chu, Y.-H., et al. 2000, AJ, 119, 292
Carpenter, J. M., Snell, R. L., Schloerb, F. P., & Skrutskie, M. F. 1993, ApJ, 407, 657
Carpenter, J. M., Meyer, M. R., Dougados, C., Strom, S. E., & Hillenbrand, L. A. 1997, AJ, 114, 198
Casali, M. M., & Hawarden, T. G. 1992, JCMT-UKIRT Newsl., 4, 33
Clayton, C. A. 1986, MNRAS, 219, 895
Clayton, C. A. 1990, MNRAS, 246, 712
Crowther, P. A., & Dessart, L. 1998, MNRAS, 296, 622
De Pree, C. G., Nysewander, M. C., & Goss, W. M. 1999, AJ, 117, 2902
Djorgovsky, S., & King, I. R. 1986, ApJ, 305, L61
Drissen, L., Moffat, A. F. J., Walborn, N. R., & Shara, M. M. 1995, AJ, 110, 2235
Eisenhauer, F., Quirrenbach, A., Zinnecker, H., & Genzel, R. 1998, ApJ, 498, 278 (E+98)
Elmegreen, B. G. 2000, ApJ, 530, 277
Elmegreen, B. G., Efremov, Y. N., Pudritz, R. E., & Zinnecker, H. 2000, in Protostars and Planets IV, ed. V. Mannings, A. P. Boss, & S. S. Russell, 179
Frogel, J. A., Persson, S. E., & Aaronson, M. 1977, ApJ, 213, 723
Goss, W. M., & Radhakrishnan, V. 1969, ApL, 4, 199
Goss, W. M., Radhakrishnan, V., Brooks, J. W., & Murray, J. D. 1972, ApJS, 24, 123
Hillenbrand, L. A. 1997, AJ, 113, 1733
Hillenbrand, L. A., & Hartmann, L. W. 1998, ApJ, 492, 540
Hofmann, K.-H., Seggewiss, W., & Weigelt, G. 1995, A&A, 300, 403
Jones, T. J., Ashley, M., Hyland, A. R., & Ruelas-Mayorga, A. 1981, MNRAS, 197, 413
Kaluzny, J., & Udalski, A. 1992, Acta Astron., 42, 29
Kennicutt, R. C. 1984, ApJ, 287, 116
King, I. R. 1962, AJ, 67, 471
King, I. R. 1966, AJ, 71, 276
King, I. R., Hedemann, E., Hodge, S. M., & White, R. E. 1968, AJ, 73, 456
Lada, E. A., DePoy, D. L., Evans, N. J., & Gatley, I. 1991, ApJ, 371, 171
Lada, C. J., DePoy, D. L., Merrill, K. M., & Gatley, I. 1993a, ApJ, 374, 533
Lada, C. J., Young, E. T., & Green, T. P. 1993b, ApJ, 408, 471
Megeath, S. T, Herter, T., Beichman, C., et al. 1996, A&A, 307, 775
Melnick, J., Tapia, M., & Terlevich, R. 1989, A&A, 213, 89
Meyer, M. R., Adams, F. C., Hillenbrand, L. A., Carpenter, J. M., & Larson, R. B. 2000, in Protostars and Planets IV, ed. V. Mannings, A. P. Boss, & S. S. Russell, 121
Meylan, G., & Pryor, C. 1993, in Structure and Dynamics of Globular Clusters, ed. S. G. Djorgovski, & G. Meylan, ASP Conf. Ser., 50, 31
Miller, G. E., & Scalo, J. M. 1979, ApJS, 41, 513
Moffat, A. F. J. 1974, A&A, 35, 315

Moffat, A. F. J. 1983, A&A, 124, 273
Moffat, A. F. J., Drissen, L., & Shara, M. M. 1994, ApJ, 436, 183
Mücke, A., Koribalski, B., Moffat, A. F. J., Corcoran, M. F., & Stevens, I. R. 2002, ApJ, subm.
Nürnberger, D. E. A. 2002a, Ph.D. Thesis, University Würzburg, in prep.
Nürnberger, D. E. A. 2002b, in Hot Star Workshop III: The Earliest Phases of Massive Star Birth, ASP Conf. Ser., ed. P. A. Crowther, in press
Nürnberger, D., Bronfman, L., Petr-Gotzens, M., & Stanke, Th. 2002a, in The Origin of Stars and Planets: The VLT View, ESO Astrophysics Symp. Ser., ed. J. Alves, & M. McCaughrean, in press
Nürnberger, D. E. A., Bronfman, L., Yorke, H. W., & Zinnecker, H. 2002b, A&A, in prep.
Pandey, A. K., Ogura, K., & Sekiguchi, K. 2000, PASJ, 52, 847
Persson, S. E., Murphy, D. C., Krzeminski, W., Roth, M., & Rieke, M. J. 1998, AJ, 116, 2475
Press, W. H., Flannery, B. P., Teukolsky, S. A., & Vetterling, W. T. 1989, Numerical Recipes (Cambridge University Press)
Sagar, R., Munari, U., & de Boer, K. S. 2001, MNRAS, 327, 23
Salpeter, E. E. 1955, ApJ, 121, 161
Scalo, J. M. 1986, Fundamentals of Cosmic Physics, 11, 1
Sirianni, M., Nota, A., Leitherer, C., De Marchi, G., & Clampin, M. 2000, ApJ, 533, 203
Stetson, P. B. 1987, PASP, 99, 1915
Tapia, M., Bohigas, J., Pérez, B., Roth, M., & Ruiz, M. T. 2001, RMxAA, 37, 39
Van den Bergh, S. 1978, A&A, 63, 275
Wainscoat, R. J., Cohen, M., Volk, K., Walker, H. J., & Schwartz, D. E. 1992, ApJS, 83, 111